

RESEARCH ARTICLE | AUGUST 05 2025

The dynamic impact of surging waves on coastal structures via a wave–structure coupling model

Special Collection: [Wave-Structure Interaction](#)

Pengxuan Luo (罗鹏翱)  ; Jingxin Zhang (张景新)  

 Check for updates

Physics of Fluids 37, 082106 (2025)

<https://doi.org/10.1063/5.0279462>



View
Online



Export
Citation

09 August 2025 09:35:29



Physics of Fluids
Special Topics
Open for Submissions

[Learn More](#)

 AIP
Publishing

The dynamic impact of surging waves on coastal structures via a wave-structure coupling model

Cite as: Phys. Fluids **37**, 082106 (2025); doi: [10.1063/5.0279462](https://doi.org/10.1063/5.0279462)

Submitted: 7 May 2025 · Accepted: 29 June 2025 ·

Published Online: 5 August 2025



View Online



Export Citation



CrossMark

Pengxuan Luo (罗鹏翱)¹ and Jingxin Zhang (张景新)^{1,2,a}

AFFILIATIONS

¹School of Ocean and Civil Engineering, Shanghai Jiao Tong University, Shanghai, China

²MOE Key Laboratory of Hydrodynamics, Shanghai Jiao Tong University, Shanghai, China

Note: This paper is part of the Special Topic, Wave-Structure Interaction.

^aAuthor to whom correspondence should be addressed: zhangjingxin@sjtu.edu.cn

ABSTRACT

The study of wave impact structures is a key focus of coastal protection and marine hazard mitigation. Fluid-structure coupling numerical simulation is a powerful technical method. This paper presents an integrated numerical framework combining the non-hydrostatic method with the immersed boundary method to investigate wave-structure interactions. The framework incorporates rigid body dynamics and a collision detection algorithm to resolve coupled hydrodynamic and structural interactions under wave force. A novel water elevation correction method with adaptive flux constraints at wave-structure interfaces successfully addresses mass conservation challenges during wave propagation over obstacles. Model validation through submerged bar benchmark tests demonstrates the accuracy of numerical model in wave propagation simulation. Combined wave flume experiments and parametric studies further validate the model in simulating coastal processes spanning wave generation, run-up dynamics, and structural responses. Comparative analysis reveals that simulated motion trajectories achieve good agreement with experimental measurements, particularly in capturing the effects of nonlinear wave-structure coupling. Numerical results of surge wave impacts on structures demonstrate shelter structures can reduce the impact forces by 50%, with system-scale analysis revealing stabilized force attenuation of approximately 15% under increasing structural density. An attenuation coefficient analysis quantifies the relationship between the number of sheltering structures and the reduction in wave force.

Published under an exclusive license by AIP Publishing. <https://doi.org/10.1063/5.0279462>

09 August 2025 09:35:29

I. INTRODUCTION

Waves constitute a fundamental hydrodynamic phenomenon in marine and coastal environments. The nonlinear interaction mechanisms between surge waves and coastal structures are critical scientific issues in the field of ocean engineering. Accurate and efficient numerical simulations of the wave-structure interaction processes are essential to provide reliable guidance for the design and optimization of coastal infrastructure.

Three-dimensional wave modeling requires accurate tracking of the free surface evolution. Several well-known numerical approaches, such as the volume of fluid (VOF) method,^{1,2} the level set method^{3,4} and the smoothed particle hydrodynamics (SPH) method,^{5,6} have demonstrated significant efficacy in simulating complex free surface flows. Nevertheless, the high computational cost associated with these methods limited their application in simulating large-scale wave motion with required accuracy.

In order to enhance computational efficiency, the non-hydrostatic model with terrain-following coordinate transformation

has emerged as a promising computational framework. Lin *et al.*^{7,8} proposed a model based on vertical coordinate transformation by assuming the water elevation as a single-valued function of the horizontal coordinate. Ma *et al.*^{9,10} developed a numerical model NHWAVE under non-hydrostatic conditions by incorporating the Riemann approximation for computing the cell surface flux. These non-hydrostatic wave models have demonstrated robust capabilities in simulating wave propagation, run-up, and inundation processes in coastal environments.^{11–13}

In addressing the issue of wave-structure interactions, Lin⁷ and Chen *et al.*¹⁴ proposed an advanced model featuring multi-layered vertical coordinate transformation to accurately represent the positions of suspended structures. While this approach successfully simulated submerged and floating cubic bodies, it entailed substantial numerical implementation complexity. Other studies mainly focused on the treatment of static structures of vertically emergent structures.^{15–17} However, submerged and moving structures in flow fields remain a persistent challenge for non-hydrostatic models.

Conventional body-fitted meshes have been shown to engender significant computational complexity and to result in discontinuities of vertical coordinates.

The immersed boundary method (IBM) has emerged as an innovative computational framework for addressing complex wave-structure interaction problems. The fundamental principle of IBM is to incorporate volumetric forcing terms into the momentum equations to simulate the influence of physical boundaries.¹⁸ These volumetric forces, commonly referred to as virtual boundary forces, effectively eliminate the complexity of body-fitted mesh generation. Goldstein *et al.*¹⁹ introduced the feedback forcing approach, which implements no-slip boundary conditions through velocity-correcting feedback forces. Fadlun *et al.*²⁰ and Mohd-Yusof²¹ developed a boundary velocity interpolation scheme, enabling the imposition of boundary conditions on interfaces that do not align with the computational mesh. In the ghost cell methodology employed by Tseng and Ferziger,²² virtual boundary forces were calculated by boundary velocity interpolation at each time step. This approach was adopted to ensure that the no-slip velocity boundary condition was satisfied at ghost cells. Mittal *et al.*^{23,24} implemented a sharp interface immersed boundary method within a three-dimensional finite volume framework, incorporating a trilinear interpolation method for boundary velocity estimation at ghost cells. Extensive studies have validated that linear interpolation schemes achieve an optimal balance between computational efficiency.^{25–28}

Recent advancements in the application of the immersed boundary method to free surface flows have significantly extended its scope of applicability. Shen and Chan,^{29,30} demonstrated the efficacy of integrating IBM with the VOF method, enabling accurate simulations of solitary wave propagation across continental shelves and progressive wave interactions with steeply sloping submerged breakwaters. Yang and Stern³¹ combined the classical level set method for fluid-fluid interface tracking with IBM for fluid-solid interactions, facilitating simulations of waves generated by landslides and moving vessels. Zhao *et al.*³² effectively employed IBM to model bridge structures with complex geometric boundaries, making progress in numerical simulations of tsunami wave impacts on coastal infrastructure. Ha *et al.*³³ implemented IBM for seabed topography simulation by treating irregular bathymetric variations as virtual boundaries with imposed volumetric forces, thereby accurately replicating wave run-up processes. Kang *et al.*³⁴ established a multi-layer vertical grid system that maintained undeformed vertical meshes near submerged structures to enhance computational stability. Ma *et al.*⁹ extended the non-hydrostatic wave model NHWAVE by incorporating IBM to address structures within flow fields and implemented a fractional step projection scheme for virtual boundary force computation. Similarly, Ai *et al.*^{35,36} used IBM to simulate wave interactions with suspended structures, validating numerical accuracy through comprehensive experimental data analysis. Yu *et al.*³⁷ investigated the wave effect on a perforated plate by using immersed boundary generalized harmonic polynomial cell method. However, present works mainly focus on static structures under wave impact, and the issues of dynamic impact of waves on moving structures have not been extensively discussed.

The paper is organized systematically as follows: First, the governing equations and numerical schemes for the fluid and solid solvers

are introduced in detail in Sec. II. Then, the performance of the model is rigorously evaluated through the validation benchmark, and the application of surge wave interaction with static and moving structures is discussed in Sec. III. Finally, the main conclusions are summarized in Sec. IV.

II. METHODOLOGY FOR NUMERICAL MODEL

A. Governing equations

The governing equations of fluid dynamics are formulated using the σ -coordinate transformed Reynolds-averaged Navier-Stokes equations. The σ -coordinate transformation method is based on the single-valued function assumption of water elevation, which enables simulation in both the free surface and the uneven bottom boundary. The transformed coordinate system can be written as follows:

$$x = x^*, \quad y = y^*, \quad \sigma = \frac{z^* - \eta}{H}, \quad t = t^*, \quad (1)$$

where $H = h + \eta$ presents the total water depth, η is the water elevation and h is the still water depth. After the coordinate transformation, the coordinate of vertical direction becomes $\sigma = [-1, 0]$, which can be shown in Fig. 1.

In the σ coordinate system, the continuity equation is transformed to the water elevation governing equation, while the pressure term in the momentum equations is decomposed into a hydrostatic pressure component induced by the water elevation and a non-hydrostatic component resulting from fluid motion. The free surface can be accurately simulated by solving the water elevation equation. The continuity and momentum equations can be rewritten as follows:

$$\frac{\partial \eta}{\partial t} + \frac{\partial q_x}{\partial x} + \frac{\partial q_y}{\partial y} + \frac{\partial q_\sigma}{\partial \sigma} = 0, \quad (2)$$

$$\frac{\partial \mathbf{Q}}{\partial t} + \frac{\partial \mathbf{C}_x}{\partial x} + \frac{\partial \mathbf{C}_y}{\partial y} + \frac{\partial \mathbf{C}_\sigma}{\partial \sigma} = \frac{\partial \mathbf{D}_x}{\partial x} + \frac{\partial \mathbf{D}_y}{\partial y} + \frac{1}{H^2} \frac{\partial \mathbf{D}_\sigma}{\partial \sigma} + \mathbf{S}, \quad (3)$$

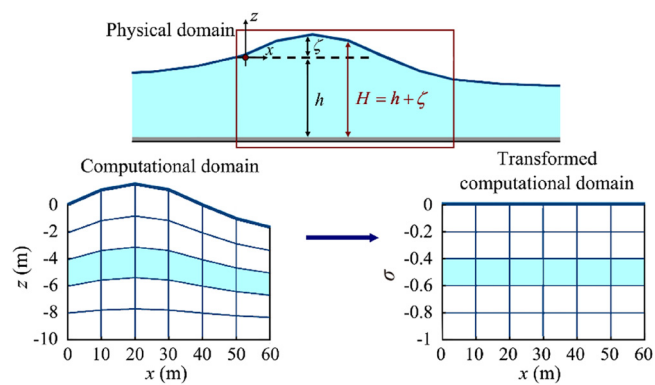


FIG. 1. Schematic of the vertical σ coordinate transformation used in the non-hydrostatic method.

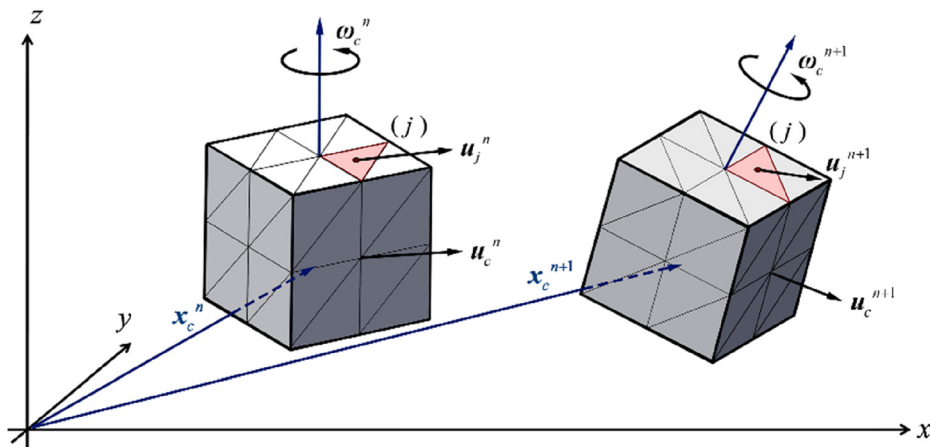


FIG. 2. Schematic of the variable representation for structure motion.

$$\begin{aligned} \mathbf{Q} &= \begin{bmatrix} Hu \\ Hv \\ Hw \end{bmatrix}, \quad \mathbf{C}_x = \begin{bmatrix} Huu \\ Hvu \\ Hwu \end{bmatrix}, \quad \mathbf{C}_y = \begin{bmatrix} Huv \\ Hvv \\ Hvw \end{bmatrix}, \\ \mathbf{C}_z &= \begin{bmatrix} Hu\tilde{w} \\ Hv\tilde{w} \\ Hw\tilde{w} \end{bmatrix}, \quad \mathbf{D}_x = \begin{bmatrix} \nu_t \frac{\partial Hu}{\partial x} \\ \nu_t \frac{\partial Hv}{\partial x} \\ \nu_t \frac{\partial Hw}{\partial x} \end{bmatrix}, \quad \mathbf{D}_y = \begin{bmatrix} \nu_t \frac{\partial Hu}{\partial y} \\ \nu_t \frac{\partial Hv}{\partial y} \\ \nu_t \frac{\partial Hw}{\partial y} \end{bmatrix}, \\ \mathbf{D}_\sigma &= \begin{bmatrix} \nu_t \frac{\partial Hu}{\partial \sigma} \\ \nu_t \frac{\partial Hv}{\partial \sigma} \\ \nu_t \frac{\partial Hw}{\partial \sigma} \end{bmatrix}, \quad \mathbf{S} = \begin{bmatrix} -gH \frac{\partial \zeta}{\partial x} - \frac{H}{\rho} \frac{\partial p_n}{\partial x} + Hf_{IBx} \\ -gH \frac{\partial \zeta}{\partial y} - \frac{H}{\rho} \frac{\partial p_n}{\partial y} + Hf_{IBy} \\ -\frac{1}{\rho} \frac{\partial p_n}{\partial \sigma} + Hf_{IBz} \end{bmatrix}, \end{aligned} \quad (4)$$

where vector \mathbf{Q} , \mathbf{C} , \mathbf{D} , and \mathbf{S} represent the flow terms, convective terms, diffusion terms and source terms, respectively. The virtual boundary force term f_{IB} is introduced into the momentum equations to emulate the immersed boundary and the eddy viscosity coefficient ν_t is solved by the two-equation SST $k-\omega$ turbulence model.³⁸ For the sake of clarity, variables $\mathbf{q}_x = Hu$, $\mathbf{q}_y = Hv$, and $\mathbf{q}_z = Hw$ represent the flux in the x , y , and z directions, respectively. Another flow variable \mathbf{q}_σ represents the flux in the vertical σ coordinate and is calculated as follows:

$$\begin{aligned} q_\sigma &= -\left(\frac{\partial \eta}{\partial t} + \sigma \frac{\partial H}{\partial t}\right) - \frac{q_x}{H} \left(\frac{\partial \eta}{\partial x} + \sigma \frac{\partial H}{\partial x}\right) \\ &\quad - \frac{q_y}{H} \left(\frac{\partial \eta}{\partial y} + \sigma \frac{\partial H}{\partial y}\right) + \frac{q_z}{H}. \end{aligned} \quad (5)$$

The governing equations of solid structure motion are formulated according to Newtonian kinematic laws. In this study, the structure is modeled as a rigid body. The general motion of the structures can be kinematically decomposed into translational motion and rotation around the center of mass at a fixed point.

$$m \frac{d\mathbf{u}}{dt} = \mathbf{f}_v + \mathbf{f}_s, \quad (6)$$

$$I \frac{d\omega}{dt} = \mathbf{r} \times (\mathbf{f}_v + \mathbf{f}_s), \quad (7)$$

where m and I represent the mass and moment of inertia of the structure, and \mathbf{f}_v and \mathbf{f}_s represent the total volume force and the total surface force on the structure, respectively. When the structure is moving, \mathbf{u} and ω represent the velocity and angular velocity of the center of mass, which is shown in Fig. 2

B. Numerical schemes for fluid solver

For the free surface flow, the non-hydrostatic method is employed to simulate variations in water elevation. The immersed boundary method is used to address issues related to wave–structure interaction. The fundamental concept is to apply virtual boundary forces within the governing equations to simulate the influence of physical boundaries. In this study, the computational domain is divided into fluid area, solid area, and immersed boundary (IB) area, as shown in Fig. 3. Virtual boundary forces are applied on the cells in IB area to satisfy the boundary conditions.

To discretize the governing equations, a semi-implicit scheme for time integration is implemented with the aid of a weighting parameter

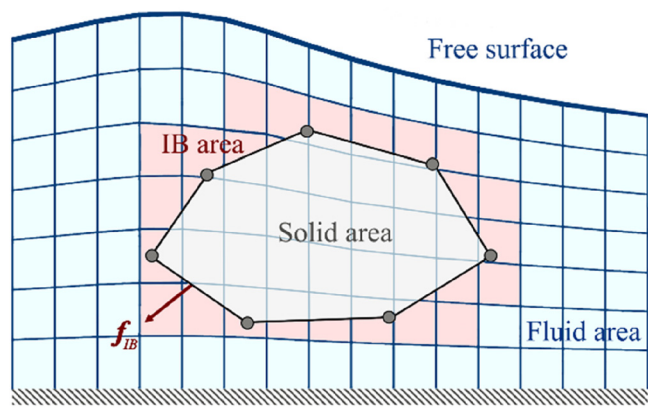


FIG. 3. Schematic of the immersed boundary method and cell classification in computational domain.

θ ranging in [0,1], and a constant value $\theta = 0.5$ is used in present study. Under a CFL condition $u\Delta t/\Delta x < 1$, the semi-implicit scheme for time integration exhibits good numerical stability. A second-order TVD scheme is employed to manage this spatial discretization.³⁹ The discretized governing equations, including both the continuity and momentum equations, are formally expressed by the following forms:

$$\frac{\eta_{i,k}^{n+1} - \eta_{i,k}^n}{\Delta t} + \theta \sum_{k=1}^{NK} (\sigma_k \nabla \cdot \mathbf{q}_{i,k}^{n+1}) + (1-\theta) \sum_{k=1}^{NK} (\sigma_k \nabla \cdot \mathbf{q}_{i,k}^n) = 0, \quad (8)$$

$$\begin{aligned} \frac{\mathbf{q}_{i,k}^{n+1} - \mathbf{q}_{i,k}^n}{\Delta t} + \mathbf{C}_{i,k}^n + \mathbf{D}_{i,k}^{n+1} - gH[\theta \nabla \eta_{i,k}^{n+1} + (1-\theta) \nabla \eta_{i,k}^n] \\ - \frac{H}{\rho} \nabla p_{n,i,k}^{n+1} + Hf_{IBi,k} = 0, \end{aligned} \quad (9)$$

where σ_k denotes the height of vertical layer, and the vector f_{IB} contains the immersed boundary force term in three-dimensional domain. We use the subscripts i, k for the mesh index and the superscript n for the time step.

These discretized equations are solved using a splitting strategy called the predictor-corrector scheme. The following steps can be used to solve Eq. (9) sequentially:

$$\mathbf{q}_{i,k}^{(1)} = \mathbf{q}_{i,k}^n - \Delta t [\mathbf{C}_{i,k}^n + gH(1-\theta) \nabla \eta_{i,k}^n + Hf_{IBi,k}], \quad (10)$$

$$\mathbf{q}_{i,k}^* = \mathbf{q}_{i,k}^{(1)} - \Delta t (\mathbf{D}_{i,k}^* + \theta gH \cdot \nabla \eta_{i,k}^{n+1}), \quad (11)$$

$$\mathbf{q}_{i,k}^{(2)} = \mathbf{q}_{i,k}^{(1)} - \Delta t H f_{IBi,k}^{(2)}, \quad (12)$$

$$\mathbf{q}_{i,k}^{n+1} = \mathbf{q}_{i,k}^{(2)} - \Delta t \left(\frac{H}{\rho} \nabla p_{n,i,k}^{n+1} \right). \quad (13)$$

The discretized equation—Eq. (10)—incorporating explicit convective terms and explicit water elevation gradients is initially solved. As all explicit terms are obtained in the preceding step, this step essentially reduces to solving a system of algebraic equations. In the predictor step, non-hydrostatic pressure terms are neglected, with only water elevation contributing to pressure effects. By combining Eq. (11) and continuity equation Eq. (8), the implicit water elevation gradients are solved. The water elevation terms are substituted into Eq. (11) to derive the intermediate velocity $\mathbf{q}_{i,k}^*$. Subsequently, in the corrector step, the non-hydrostatic pressure gradient is then implicitly resolved by coupled solution of Eqs. (13) and (8), and the corrected velocity components $\mathbf{q}_{i,k}^{n+1}$ are obtained by incorporating the non-hydrostatic pressure variations into the Eq. (13).

In particular, the virtual boundary force terms are embedded in Eqs. (10) and (12) to enforce the no-slip boundary conditions at the solid-fluid interfaces. These terms can be written in the following forms in Eqs. (10) and (12), respectively.

$$f_{IBi,k}^{(1)} = \begin{cases} -\frac{\mathbf{q}_{IBi,k}^n - \mathbf{q}_{i,k}^n}{H\Delta t} - \frac{\mathbf{C}_{i,k}^n}{H} + gH(1-\theta) \nabla \eta_{i,k}^n & \text{IB cells,} \\ 0 & \text{Others,} \end{cases} \quad (14)$$

$$f_{IBi,k}^{(2)} = \begin{cases} -\frac{\mathbf{q}_{IBi,k}^{(2)} - \mathbf{q}_{i,k}^*}{H\Delta t} & \text{IB cells,} \\ 0 & \text{Others,} \end{cases} \quad (15)$$

where \mathbf{q}_{IB} is the boundary velocity determined by the structure motion. Given that the boundary points generally do not coincide with the mesh cells, \mathbf{q}_{IB} must be reconstructed by interpolation from fluid cells.

C. Numerical schemes for boundary condition reconstruction

In the present study, an inverse distance weighting interpolation method was used to calculate the boundary velocity. The reconstruction process begins with the identifying of the closest normal distance from the IB cell to the virtual boundary, which is denoted as d . Subsequently, the image points are positioned within the fluid domain up to $2d$ from the boundary interface. A search domain of cells within three mesh lengths is defined for interpolation source selection. Reconstruction of the boundary velocity \mathbf{q}_{IB} at the IB cell is then achieved through the implementation of a linear interpolation method by estimating values from neighboring fluid cells, as shown in Fig. 4.

The variables at image points are influenced by each fluid cell within the search domain. The interpolation weight of these fluid cells and the velocity of image points can be expressed as

$$\mathbf{u}_{IP} = \sum_{m=j}^{NJ} (\lambda_j \mathbf{u}_j), \quad \lambda_j = \frac{1}{\|\mathbf{x}_j - \mathbf{x}_{IP}\|^2 + \varepsilon} \sum_{m=1}^{NM} \frac{1}{\|\mathbf{x}_m - \mathbf{x}_{IP}\|^2 + \varepsilon}, \quad (16)$$

where λ denotes the interpolation weight and the symbol ε represents a tiny perturbation parameter introduced to prevent division by zero. The subscripts j, m represent the index of fluid cells in the search domain. Then, the boundary velocity \mathbf{u}_{IB} can be obtained using a linear interpolation of the boundary velocity \mathbf{u}_{BP} and \mathbf{u}_{IP} in the following equations:

$$\mathbf{u}_{IBi,k} = \frac{1}{2} (\mathbf{u}_{BP} + \mathbf{u}_{IP}). \quad (17)$$

In the present study, the pressure boundary conditions must be taken into consideration. Given the decomposition of the pressure into hydrostatic and non-hydrostatic components, different boundary treatments are implemented for each pressure component.

The hydrostatic pressure variation is essentially induced by the water elevation, which is solved through flux integration along the vertical direction. However, submerged structures in the flow field disrupt the continuity of the vertical layers, introducing errors in the flux integration that affect the conservation of mass. To overcome this limitation, we proposed a water elevation correction method within the

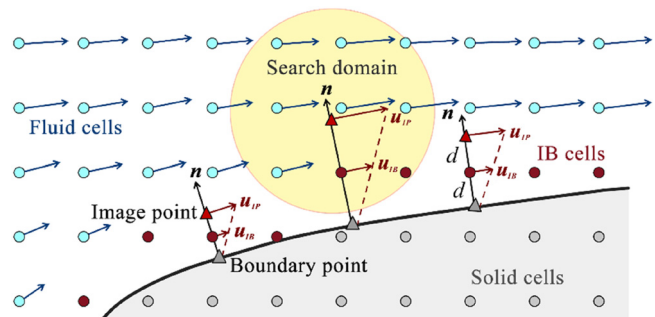


FIG. 4. Schematic of the virtual boundary velocity interpolation method on IB cells.

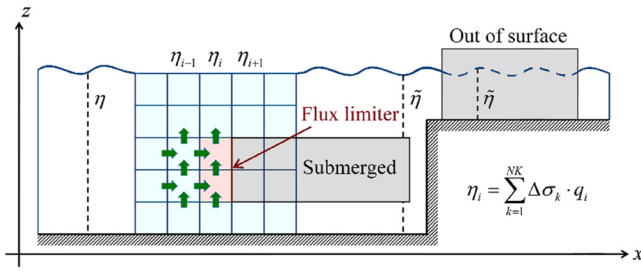


FIG. 5. Schematic of the flux limiter and water elevation correction method.

immersed boundary framework. This approach implements flow constraints on IB cells adjacent to structures that are submerged in the flow field and partially located outside the free surface, as illustrated in Fig. 5. This method eliminates mass conservation errors and improves the capability of the immersed boundary method in simulating the structure transitions from emergent to submerged states during surge inundation processes.

With regard to the non-hydrostatic pressure component, it is calculated independently for each cell, remaining independent of the integration equation. Consequently, boundary conditions on IB cells can be implemented using interpolation methods similar to those used for the virtual boundary velocity. Moreover, it is imperative to ensure that the non-hydrostatic pressure gradients are zero in the wall-normal direction at the static boundary to satisfy the no-flux boundary condition.

$$\frac{\partial p_n}{\partial n} = 0, \quad p_{n,IB} = p_{n,IP}. \quad (18)$$

The reconstruction of boundary conditions has been finalized, and the flux and pressure within the IB cell can be determined by utilizing the following equations:

$$\mathbf{q}_{IB,i,k} = \frac{H}{2} \left[\mathbf{u}_{BP} + \sum_{j=1}^{NJ} \left(\frac{1}{\|\mathbf{x}_j - \mathbf{x}_{IP}\|^2 + \varepsilon} \sum_{m=1}^{NM} \frac{1}{\|\mathbf{x}_m - \mathbf{x}_{IP}\|^2 + \varepsilon} \right) \cdot \mathbf{u}_j \right], \quad (19)$$

$$p_{nIB,i} = \sum_{j=1}^{NJ} \left(\frac{1}{\|\mathbf{x}_j - \mathbf{x}_{IP}\|^2 + \varepsilon} \sum_{m=1}^{NM} \frac{1}{\|\mathbf{x}_m - \mathbf{x}_{IP}\|^2 + \varepsilon} \right) \cdot p_{nj}. \quad (20)$$

Substituting Eq. (19) into Eqs. (14) and (15), the virtual boundary force can be solved. Subsequently, the virtual boundary force is introduced into Eqs. (10) and (12), a time step for the fluid solver is complete.

D. Numerical schemes for rigid body dynamics

The structures are resolved in the Lagrange system, and the geometry is discretized into surface elements, with the spatial index j denoting each mesh element. The discretized governing equations are formally expressed as follows:

$$m \frac{\mathbf{u}_c^{n+1} - \mathbf{u}_c^n}{\Delta t} = \sum_{j=1}^{NJ} \mathbf{f}_j^n, \quad (21)$$

$$I^n \frac{\boldsymbol{\omega}_c^{n+1} - \boldsymbol{\omega}_c^n}{\Delta t} = \sum_{j=1}^{NJ} (\mathbf{r}_j^n \times \mathbf{f}_j^n), \quad (22)$$

where the subscript c represents the variable at the center of mass of the solid, and j represents the variable at the center of the discrete surface element.

The temporal discretization remains consistent with the fluid phase and an explicit time integration scheme is used for the structure motion. Equations (21) and (22) can be solved and the position and rotation status can be obtained simultaneously as follows:

$$\mathbf{u}_c^{n+1} = \mathbf{u}_c^n + \Delta t \frac{1}{m} \sum_{j=1}^{NJ} \mathbf{f}_j^n, \quad \mathbf{x}_c^{n+1} = \mathbf{x}_c^n + \Delta t \mathbf{u}_c^{n+1}, \quad (23)$$

$$\begin{aligned} \boldsymbol{\omega}_c^{n+1} &= \boldsymbol{\omega}_c^n + \Delta t (I^{-1})^n \sum_{j=1}^{NJ} (\mathbf{r}_j^n \times \mathbf{f}_j^n), \\ \mathbf{q}^{n+1} &= \mathbf{q}^n + \left[0, \frac{1}{2} \Delta t \boldsymbol{\omega}_c^n \right] \times \mathbf{q}^n, \end{aligned} \quad (24)$$

where \mathbf{q} is the quaternion which represents the rotation status of the structure.

In the flow field, structure collisions are primarily considered to occur between moving bodies and computational domain boundaries. In present study, the rigid body collision simulation is based on the stable impulse method, as illustrated in Fig. 6. Initially, the spatial position and velocity of the collision point p must be determined. Using the kinematic relationships, the position and velocity can be derived as follows:

$$\mathbf{x}_p^{n+1} = \mathbf{x}_c^{n+1} + \mathbf{R}^{n+1} \mathbf{r}_p^0, \quad (25)$$

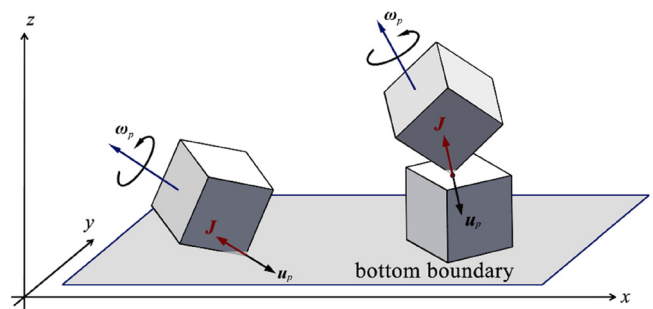
$$\mathbf{u}_p^{n+1} = \mathbf{u}_c^{n+1} + \boldsymbol{\omega}_c^{n+1} \times \mathbf{R}^n \mathbf{r}_p^0, \quad (26)$$

where the subscript c and p represent the center of mass and the contact point, respectively.

Then, according to collision theory, the collision point should progressively depart from the boundary during this time step. The post-collision velocity exhibits a reversed normal component, while the tangential component is attenuated due to frictional forces. The new velocity at the collision point can be expressed as follows:

$$\mathbf{u}_p^{n+1} = \alpha_n (\mathbf{u}_p^n \cdot \mathbf{n}_p^n) \mathbf{n}_p^n + \alpha_\tau [\mathbf{u}_p^n - (\mathbf{u}_p^n \cdot \mathbf{n}_p^n) \mathbf{n}_p^n], \quad (27)$$

where \mathbf{n} represents the normal vector of collision boundary, which points positively outward from the solid body to the fluid domain. The parameters α_n and α_τ are normal elasticity coefficient and tangential

FIG. 6. Schematic of collision simulation based on the impulse method with a collision impulse J between solid structures.

friction coefficient, respectively, which are determined based on the material properties of the rigid body. According to the impulse theorem, the velocity and angular velocity at the center of mass can be expressed as follows:

$$\mathbf{u}_c^{n+1} = \mathbf{u}_c^n + \frac{1}{m} \mathbf{J}^{n+1}, \quad (28)$$

$$\omega_c^{n+1} = \omega_c^n + (\mathbf{I}^{-1})^n (\mathbf{R}^n \mathbf{r}_j^0 \times \mathbf{J}^{n+1}). \quad (29)$$

Combining Eqs. (26)–(29), the new velocity at the collision point can be written in a different form

$$\mathbf{u}_p^{n+1} = \mathbf{u}_p^n + \frac{1}{m} \mathbf{J}^{n+1} - \mathbf{R}^n \mathbf{r}_p^0 \times [(\mathbf{I}^{-1})^n (\mathbf{R}^n \mathbf{r}_p^0 \times \mathbf{J}^{n+1})]. \quad (30)$$

Substituting Eq. (27) into Eq. (30), the impulse \mathbf{J}^{n+1} caused by collision can be obtained.

III. NUMERICAL CASES AND RESULTS

A. Linear wave propagation over a submerged bar

In this study, the accuracy of a numerical model in simulating wave–structure interactions was validated by a benchmark case of linear wave propagation over a submerged bar. As incident waves propagate over the bar, higher-order harmonics are generated due to abrupt variations in water depth, creating complex wave transformation patterns. Previous work by Beji and Battjes⁴⁰ provided extensive experimental data for numerical validation.

The numerical setup for this case is illustrated in Fig. 7. In this case, the total length of the bar is $L = 11$ m and the crest height is $D = 0.3$ m. The front slope is 6 m long horizontally with a gradient of 1:20, while the rear slope is 3 m long with a steeper gradient of 1:10.

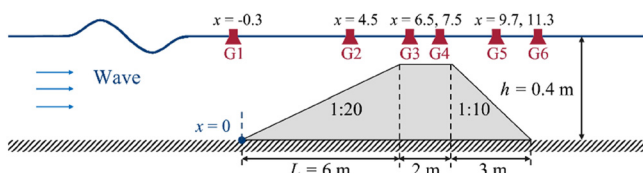


FIG. 7. Numerical setup for linear wave propagation over a submerged bar.

The top of the bar extends 2 m horizontally and sits 0.1 m below the free surface.

A linear sinusoidal wave with a wave height of $H = 0.01$ m and a period of $T = 2.02$ s was selected in this case. To monitor the complete process of wave propagation over the bar, six wave gauges were positioned along the central axis of the computational domain at the front, top, and back of the slope, respectively.

Figure 8 shows successive snapshots of wave propagation over a submerged bar. Prior to the influence of the structure, the waveform retains its regularity. During the interaction phase, the progressive shallowing of the water at the leading edge of the bar induces a gradual evolution of the waveform, culminating in noticeable deformation at the crest region with prominent high elevations. Subsequently, the transmitted waves exhibit pronounced nonlinear characteristics with increased wave steepness downstream of the structure.

Numerical simulations were performed using three sets of Cartesian meshes to verify the mesh convergence, with the mesh sizes of $\Delta x = 0.2$, 0.1, and 0.05 m. The dimensionless mesh sizes relative to the wavelength are $\Delta x/\lambda = 0.05$, 0.025, and 0.0125, respectively, and the dimensionless time step relative to the wave period is $\Delta t/T = 0.005$. It is evident that both of these parameters possess sufficient resolution for wave simulation. Figure 9 presents the comparison between simulated time series of water elevation and the corresponding experimental data collected by wave gauges.

As shown in Fig. 9, three sets of meshes demonstrate good convergence of the computational results. The root mean square errors between the numerical results and the experimental data for the three sets of meshes in one period of the sinusoidal wave are 0.093, 0.057, and 0.026, respectively. The wave gauge G1, located at the leading edge of the bar, recorded a complete waveform in Fig. 9(a). In this region, the waves are not disturbed by the bar and continue to propagate steadily. In contrast, wave gauges G2–G4 were located at the top side of the bar, where the water depth was at its shallowest. The waveforms exhibited by wave gauges G2–G4 are skewed due to the reduced water depth at this point, as shown in Figs. 9(b)–9(d). This results in a shorter wavelength compared to the waveforms captured by wave gauges located at the leading edge of the bar.

The change of waveform reflects the effect of water depth on wave propagation characteristics, particularly in areas where the water depth changes drastically. As the waves propagate toward the locations

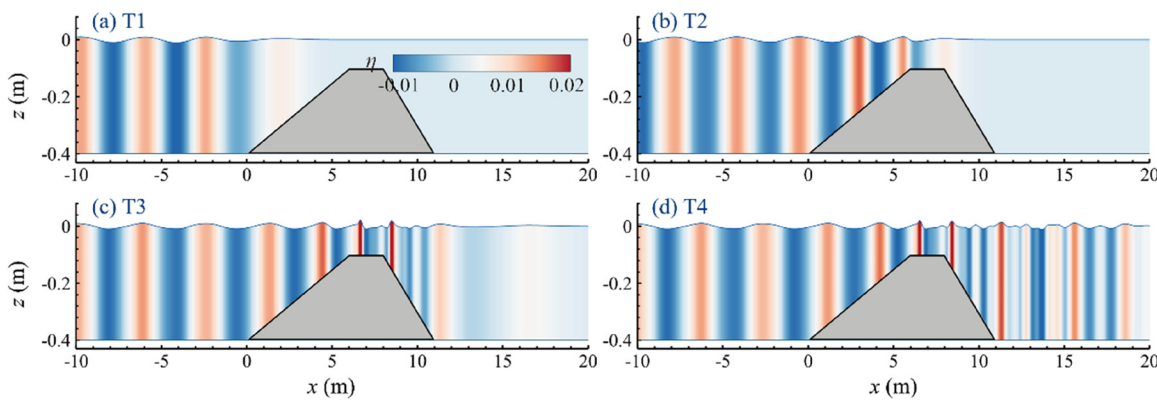


FIG. 8. Simulated free surface variation as the wave passes the top of the submerged bar at several representative times.

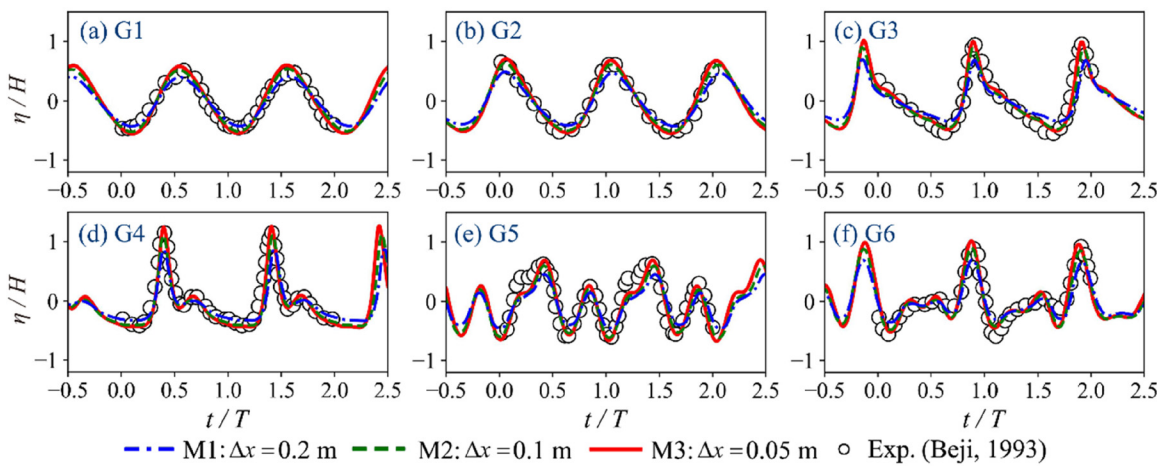


FIG. 9. Comparison of numerical and experimental time series of water elevations at gauging positions.

of wave gauges G5 and G6, the sharp change in slope and the gradual increase in water depth produce nonlinear waves, resulting in a more complex process of wave evolution, as shown in Figs. 9(e) and 9(f). Overall, the numerical results show a good agreement with experimental data. The model demonstrate its adaptability in dealing with the problem of wave propagation under non-regular submerged structures.

B. Dynamic impact of static structures under surge wave loading

In coastal regions, the process of surge wave run-up and its interaction with marine structures is a classic problem of wave–structure interaction. High-fidelity numerical modeling of this phenomenon is essential for optimizing coastal protection infrastructure design. Based on the comprehensive experimental data from large-scale wave flume tests conducted by Moris *et al.*,⁴¹ this study uses the numerical model to investigate the impact of tsunami-like waves on coastal structures.

To ensure the accuracy and reliability of the numerical simulation, the computational domain of the numerical cases strictly corresponds to the physical dimensions of the wave flume. The numerical setup is illustrated in Fig. 10. The length of the numerical flume is $L = 50$ m and the width is $W = 3$ m. The slope is 20 m long horizontally with a gradient of 1:20, and the still water depth is $h = 1$ m. The leading edge of the structures is 1.6 m from the crest of the slope. The structures are arranged with a transverse spacing of 0.6 m and a longitudinal spacing of 0.4 m between adjacent columns. The dimensionless mesh sizes relative to the structure is $\Delta x/d = 0.05$, and the

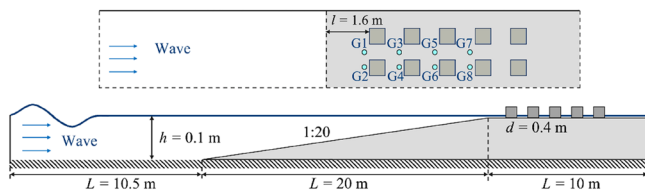


FIG. 10. Numerical setup for surge wave interaction with structures.

dimensionless time step relative to the characteristic parameter of solitary wave is $\Delta t/\sqrt{gh} = 0.005$.

Figure 11 shows the simulated flow field from the established numerical model. Figures 11(a) and 11(b) reveal the pronounced surge wave run-up dynamics along the upstream face of the first row of structures. The model accurately captures the water-blocking effect induced by the structure, demonstrating its capability in resolving hydrodynamic interactions at the leading edge during wave impact. In Figs. 11(c) and 11(d), the velocity field exhibits two distinct regimes. The flow velocity remains relatively stable in the channel regions between adjacent structures, while a significant velocity reduction is observed in the transition zones before and after the structures. Notably, the specular wave reflection observed ahead of the first structural row confirms the presence of effective energy dissipation mechanisms, which in turn provide sheltering effects for downstream structures.

Figure 12 shows a comparison of numerical and experimental time series of water elevation. Measurements from two monitoring points at the same horizontal position reveal that the water elevation at the upstream face of the structures is significantly higher than the elevation between adjacent structure rows. This phenomenon is consistent with the blocking effect of the structures on the flow, manifested as a gradual attenuation of water elevation along the flow direction.

As shown in the simulation results, a gradual reduction in peak water elevation is observed at the monitoring points located between the structure rows (subplots G1, G3, and G5). The maximum water elevation exhibited a decline of 37.1% and 12.2% from G1 to G3 and from G3 to G5, respectively. This phenomenon can be attributed to the progressive attenuation of wave energy due to lateral structure confinement, as well as turbulent dissipation as waves propagate through the structure gaps. At monitoring points positioned in front of the windward side of structures (subplots G2, G4, and G6), the numerical results demonstrate distinct peak regions in water elevation, indicating rapid water run-up processes when the flow impacts the structures.

Similarly, the maximum water elevation exhibited a decline of 24.1% and 17.2% from G2 to G4 and from G4 to G6, respectively. Notably, the data from the foremost monitoring point G2, which captures the initial wave impact on the first structure row, shows a

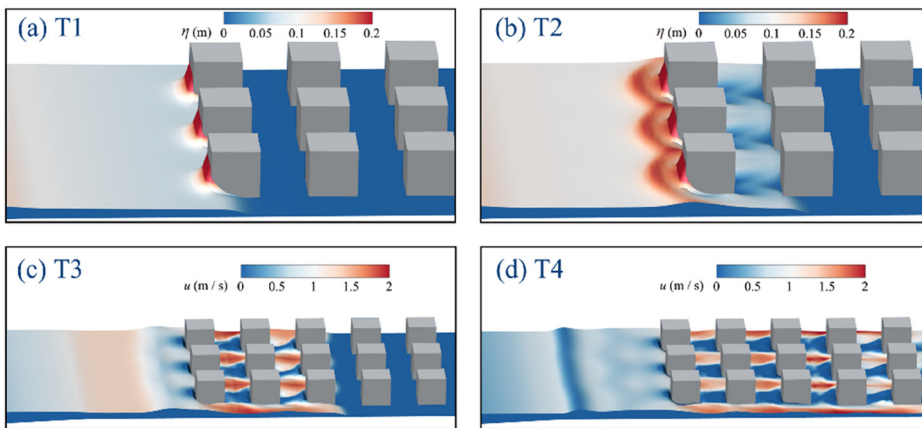


FIG. 11. The contour of simulated transient flow field as the wave passes through structures.

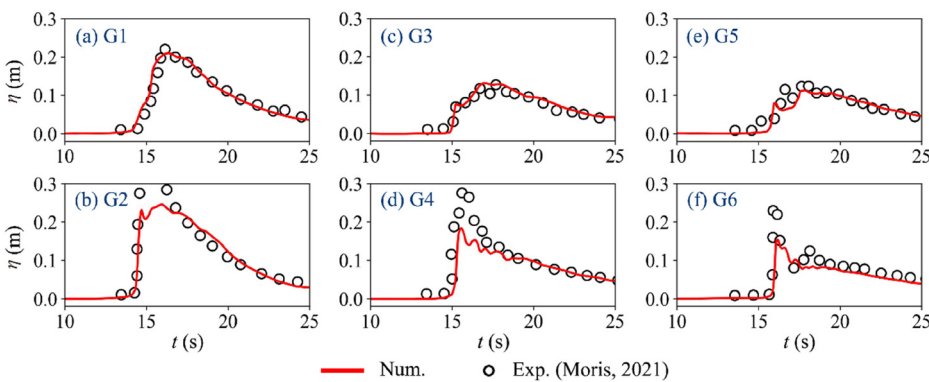


FIG. 12. Comparison of numerical and experimental time series of water elevation for wave propagation passing through structures.

09 August 2025 09:35:29

significantly longer duration of peak water elevation compared to subsequent points G4 and G6 due to concentrated wave energy. In contrast, the subsequent monitoring points located in transition zones between structure rows exhibit rapid attenuation of peak water elevation, indicating reduced hydrodynamic intensity resulting from energy dissipation by upstream structures.

It is noteworthy that the simulated water elevations at these locations are generally lower than the experimental measurements, although the timing of the peaks is in good agreement with the experimental data. This discrepancy can be attributed to the limitations of numerical simulations in capturing transient variations during wave breaking.

Furthermore, numerical results of wave force on structures and experimental data are shown in Fig. 13. The numerical results demonstrate that the maximum wave force on structures occurs at initial contact with the leading edge of the wave crest and subsequently undergoes rapid attenuation during wave propagation. Figure 13(a) shows that the simulated maximum wave force on the first row of structures is significantly lower than the experimental value, primarily due to the limitations in simulating intense wave breaking phenomena and the transient impact loads. As shown in Figs. 13(c)–13(e), the experimental data exhibit distinct periodic fluctuations, likely caused by multiple wave reflections within structures, while the present numerical model has inherent limitations in capturing such high-frequency components. Figure 13(f) shows the maximum wave force

on each row of structures during wave impact. The peak forces on the last three rows are significantly lower than those on the first two rows, indicating effective wave sheltering effects provided by the front rows. Notably, under multiple sheltering effects, the force attenuation on the rear rows demonstrates pronounced nonlinear characteristics.

In order to quantitatively assess the influence of sheltering effects under surge wave loading, this study employs a dimensionless parameter Load Reduction Factors A (LRFA) proposed by Moris *et al.*⁴¹ to describe wave force attenuation. This parameter effectively characterizes the force attenuation experienced by structures under varying degrees of sheltering and no sheltering conditions, as expressed in the following equation:

$$LRFA_j^{(i)} = \frac{F_{j,\max}^{(i)}}{F_{0,\max}^{(i)}}, \quad (31)$$

where $F_{j,\max}^{(i)}$ represents the maximum wave force exerted on structures located in the row i when sheltered by j rows of upstream structures, while $F_{0,\max}^{(i)}$ denotes the maximum wave force experienced by the structure at the same position without sheltering effect.

Figure 14 demonstrates the influence of varying numbers of sheltering rows on the wave force attenuation coefficient LRFA. Shifting the structure row rearward along the vertical axis for a fixed number of sheltering rows j significantly increases wave force attenuation, which highlights the positional dependence of sheltering efficacy. Increasing

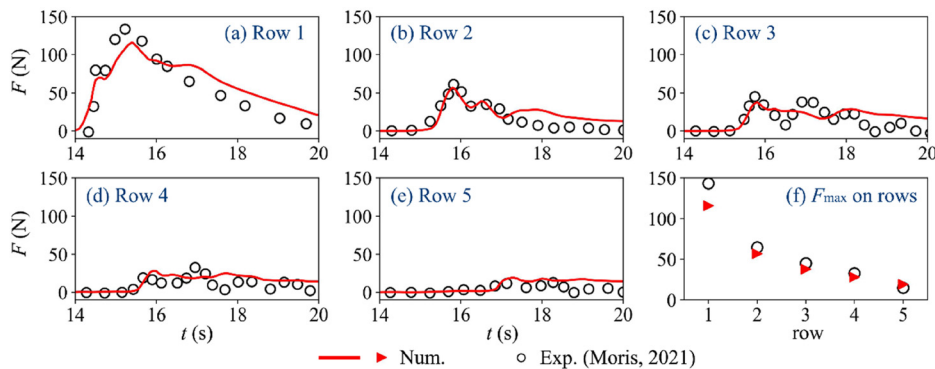


FIG. 13. Comparison of numerical and experimental time series of wave forces on structures.

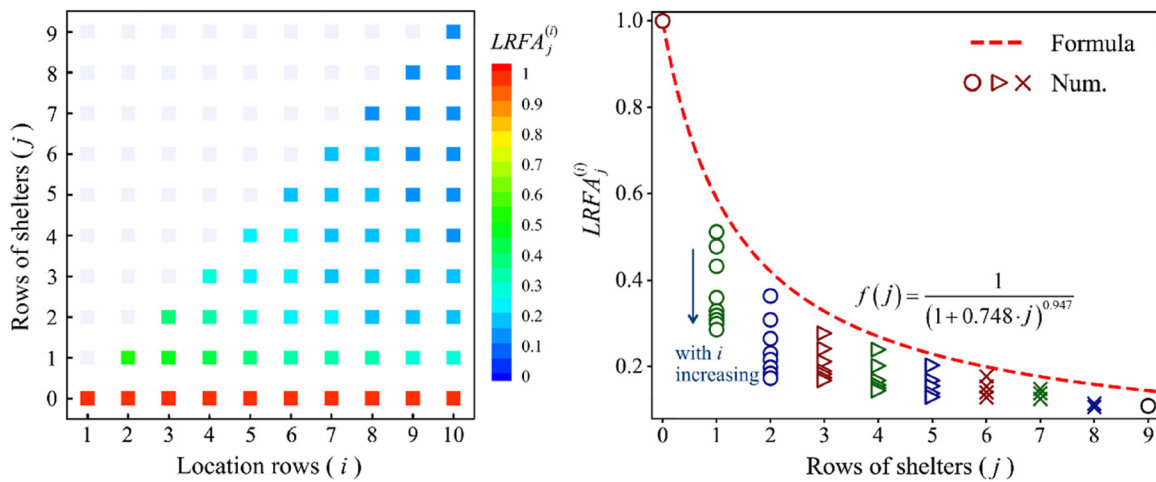


FIG. 14. Numerical results of LRFA under different rows of shelters for structures located at different locations.

the number of upstream sheltering rows j along the horizontal axis progressively reduces in LRFA values, confirming that additional sheltering structures substantially improve force attenuation.

Figure 14 provides further elucidation on the nonlinear characteristics of sheltering effects. For structures at any row, the wave force attenuation coefficient only reaches at 50% of its maximum possible attenuation value as the number of sheltering rows increases. This indicates that the rear rows are influenced not only by the sheltering effect of the upstream rows but also by energy dissipation due to bottom friction during wave run-up. As the number of sheltering rows increases, the contribution of sheltering effect to wave energy attenuation gradually exceeds that of bottom friction.

Furthermore, as the number of sheltering rows increases, the LRFA of structures within the same row exhibits a convergent trend. This indicates that in the rear region of the structure rows, the sheltering effect becomes the dominant factor, while the influence of bottom friction diminishes. As the number of sheltering rows continues to increase, however, the marginal benefit of the sheltering effect demonstrates a decreasing trend, implying that the effective sheltering rate gradually approaches saturation. This observation is consistent with the findings that the wave force attenuation coefficient has a distinct upper limit.^{41–43} The fitted curves in Fig. 14 validate this behavior, and

the numerical simulation results presented in this study further support this conclusion.

C. Dynamic impact of moving structures under surge wave loading

Numerical simulations of the dynamic impact of structures under wave loading involve a wide range of physical processes, including wave evolution, free surface deformation tracking, moving boundary coupling and multi-body collision mechanisms. In this section, the capability of numerical model in simulating the complete process of wave generation, propagation, run-up and subsequent structural interactions is evaluated comprehensively.

To ensure the accuracy and reliability of the numerical model validation process, the computational domain of the numerical cases strictly corresponds to the physical dimensions of the wave flume. The numerical setup is illustrated in Fig. 15. The length of the numerical flume is $L = 1.85$ m and the width is $W = 0.16$ m. The slope is 0.5 m long horizontally with a gradient of 1:10, and the still water depth is $h = 0.05$ m. The dimensionless mesh sizes relative to the structure is $\Delta x/d = 0.05$, and the dimensionless time step relative to the characteristic parameter of solitary wave is $\Delta t/\sqrt{gh} = 0.001$. The wave paddle

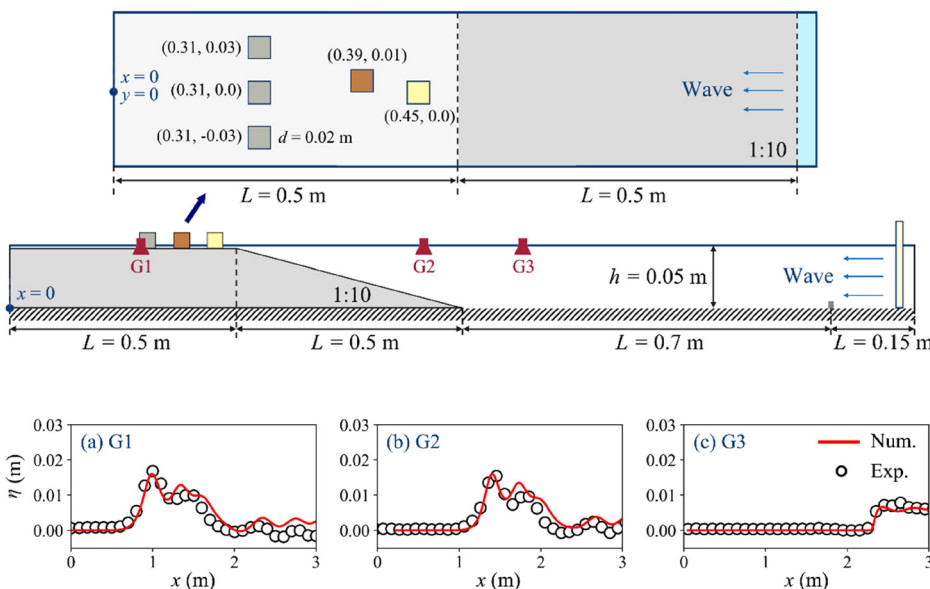


FIG. 15. Experimental wave flume diagram and numerical setup for the wave flume.

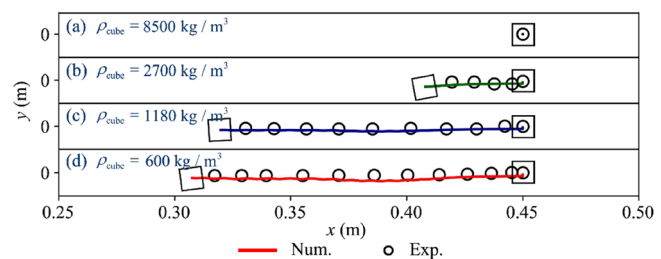


FIG. 17. Comparison of simulated moving trajectories of structures with different densities and experimental measurements from $t = 0$ to $t = 3$ s.

with a maximum velocity of $u = 0.15$ m/s could generate a solitary wave in the experiment.

In the experiment, four cubic structures with an edge length of 0.02 m were selected for analysis. The structures were composed of brass, aluminum, polymethyl methacrylate (PMMA) and pinewood, each with a different density. The initial position of each cube was determined by the coordinates $(x, y) = (0.45, 0)$ m, as illustrated in Fig. 15. This positioning ensured sufficient wave impact energy to induce structural movement after wave run-up while avoiding the premature dissipation of wave energy.

At first, three wave gauges at $x = 0.3$, 0.9 , and 1.2 m measured the time series of water elevation during wave generation, as shown in Fig. 16. Figures 16(a) and 16(b) show that waveforms remain unchanged prior to wave run-up, and Fig. 16(c) shows the water elevation variation after the wave arrives onshore. The numerical model shows good agreement with the experimental observations. The entire process of wave generation and propagation can be simulated by the present model.

Subsequently, numerical simulations were conducted to investigate the dynamic response characteristics of a single structure, with a systematic analysis of density effects on motion trajectories. As shown in Fig. 17, the simulated trajectories of cubes with different densities under wave loading show good agreement with experimental measurements. With regard to horizontal displacement along the x -axis, the high-density brass cube remained static under wave loading, while the aluminum cube exhibited limited sliding motion. In contrast, both PMMA and pinewood cubes exhibited significant mobility when subjected to wave forces. This phenomenon can be explained by the fact that wave forces are insufficient to overcome the static friction threshold of high-density cubes but exceed the static friction threshold of low-density cubes. Concurrently, the larger displacement of the wooden cube is also attributable to its lower inertia, despite experiencing similar wave forces.

It is noteworthy that systematically larger final displacements were consistently predicted in all cases compared to experimental

measurements. This discrepancy can be attributed primarily to simplifications in the modeling of contact friction mechanisms. The Coulomb friction function used in the present model does not adequately account for the effects of wet friction induced by variations in surface roughness, which leads to an underestimation of the average friction forces throughout the motion process.

In Fig. 18, the flow field variations during wave impact for the brass and pinewood cube are demonstrated. The images presented in the lower half of the figure are measured by a high-speed camera. The grid markings on the plate were set at uniform intervals of 0.02 m with a view to facilitate observation during the experiment.

In this case, wave forces prove insufficient to induce significant motion of brass cube, as shown in Fig. 18(a). When the wave impacted the brass cube at $t = 2.0$ s, free surface splashing emerged upstream of the brass cube due to substantial flow resistance, accompanied by rapid wave propagation around the cube. By $t = 2.15$ s, the flow passed around the cube and reunited downstream at $x = 3d$ (where d represents the length of cube), forming an elevated water crest at the convergence point.

In comparison with physical experiments, the numerical model predicts a flow convergence position that is notably delayed. This

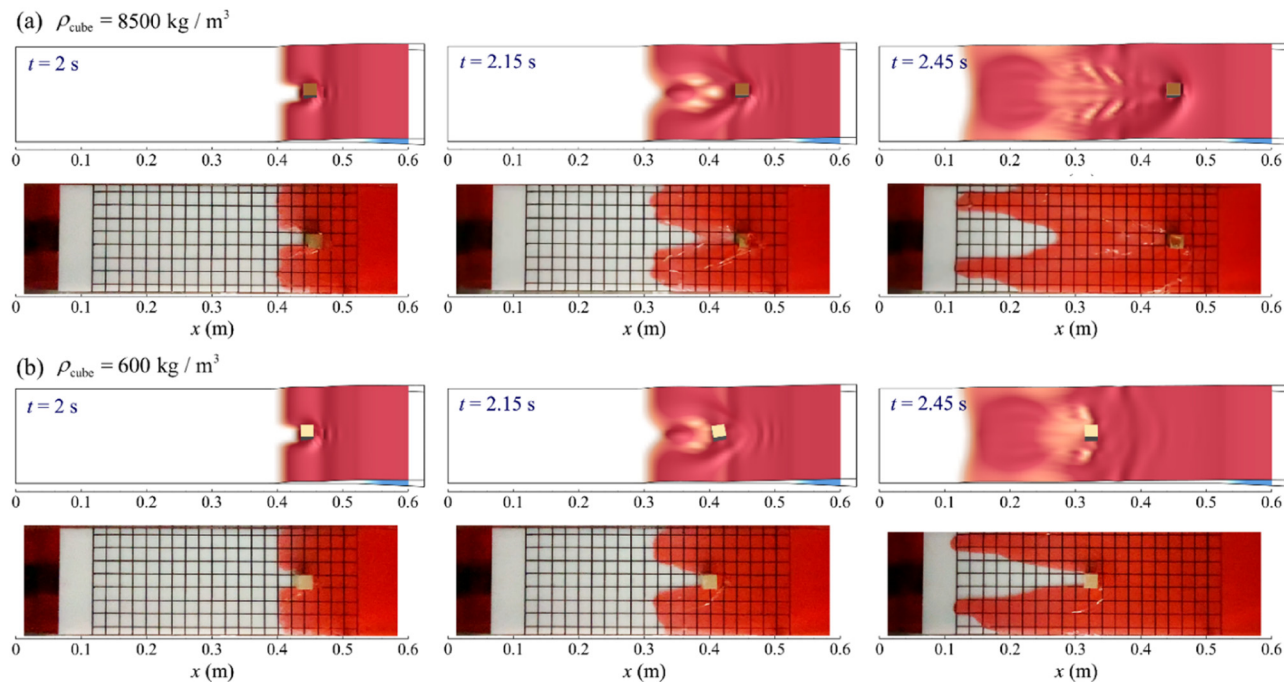


FIG. 18. Comparison of simulated moving trajectories of the single structure and wave–structure interaction flow field with experimental measurements.

discrepancy is primarily attributable to the simplified treatment of surface tension effects in the numerical model. Furthermore, the simulation results indicate the formation of ship wave patterns in the wake region behind the brass cube. The formation of these waves is attributed to the velocity differential between the cube and the fluid flow, a mechanism analogous to the formation of ship-generated waves.

In the case of the lower-density pinewood cube, the displacement induced variation in flow field structure is shown in Fig. 18(b). Numerical simulations and experimental results demonstrate that intense wave splashing does not develop upstream of the cube, nor do analogous bow wave patterns emerge in its wake, since the pinewood cube moves in conjunction with the water flow. The trajectory of the pinewood cube as it moves through space is closely aligned with experimental observations made from $t = 2.15$ to $t = 2.45$ s. The numerical model exhibits limitations in reproducing free surface morphology details. Nevertheless, its predictions of flow front advancement positions show satisfactory agreement with experimental measurements.

Figure 19 shows the moving trajectories of structures with different density under surge wave loading. At first, the pinewood cube gradually loses stability under wave loading and moves backward along a linear trajectory, which corresponds to the motion pattern of a single structure under wave loading, as shown in Fig. 19(b). At $t = 2.1$ s, the first collision occurs between the pinewood cube and the brass cube. Due to the collision point being approximately 0.01 m offset from the center of mass, the pinewood cube exhibits significant clockwise rotation and displacement along the negative y -axis. As shown in Fig. 19(c), this collision results in changes to the angular orientation and positional relationship of the structures. During post-collision motion, the pinewood cube continues negative y -axis movement driven by wave forces while maintaining rotational motion. This

kinematic characteristic is closely associated with the velocity distribution in the wake flow field behind the brass cube.

From $t = 2.1$ to $t = 2.5$ s, the pinewood cube follows the surge wave propagation around the brass cube, sustaining its negative y -axis movement. The simulated rotation angles of the pinewood cube exhibit a good agreement with experimental measurements. As shown in Fig. 19(e) and 19(f), the aluminum cube located downstream remains stationary due to the dissipation of wave energy during its shoreward propagation. Consequently, it effectively obstructs the approaching pinewood cube after a temporal interval of $t = 2.5$ s. By $t = 2.8$ s, the flow front had reached the flume sidewall, and the pinewood cube has stabilized in proximity to the leading edge of the downstream aluminum cube. Despite the numerical simulation demonstrated discrepancies in wave surface morphology compared to experimental observations, primarily limited by its treatment of plate surface tension effects, it successfully simulated the complex collision process with reasonable accuracy.

Figure 20 shows the comparison between the simulated motion trajectory of the pine cube and the experimental measurements. The simulated displacement trajectory of the pine cube shows remarkable agreement with the experimental data in the x - y plane, as shown in Fig. 20(a), which confirms the reliability of the model in predicting complex motion trajectories. Figures 20(b) and 20(c) shows the time series displacement in the x and y directions, respectively. The pine-wood cube undergoes clockwise rotation and moves to negative y -axis due to the eccentric collision under wave action between $t = 2.0$ and 2.6 s. Subsequent to $t = 2.6$ s, the pinewood cube enters a quasi-static equilibrium phase under the blocking effect of an aluminum cube, reaching final centroid coordinates of $x = 0.33$ and $y = -0.035$ m with a stable rotation angle of about 44° . The numerical simulation

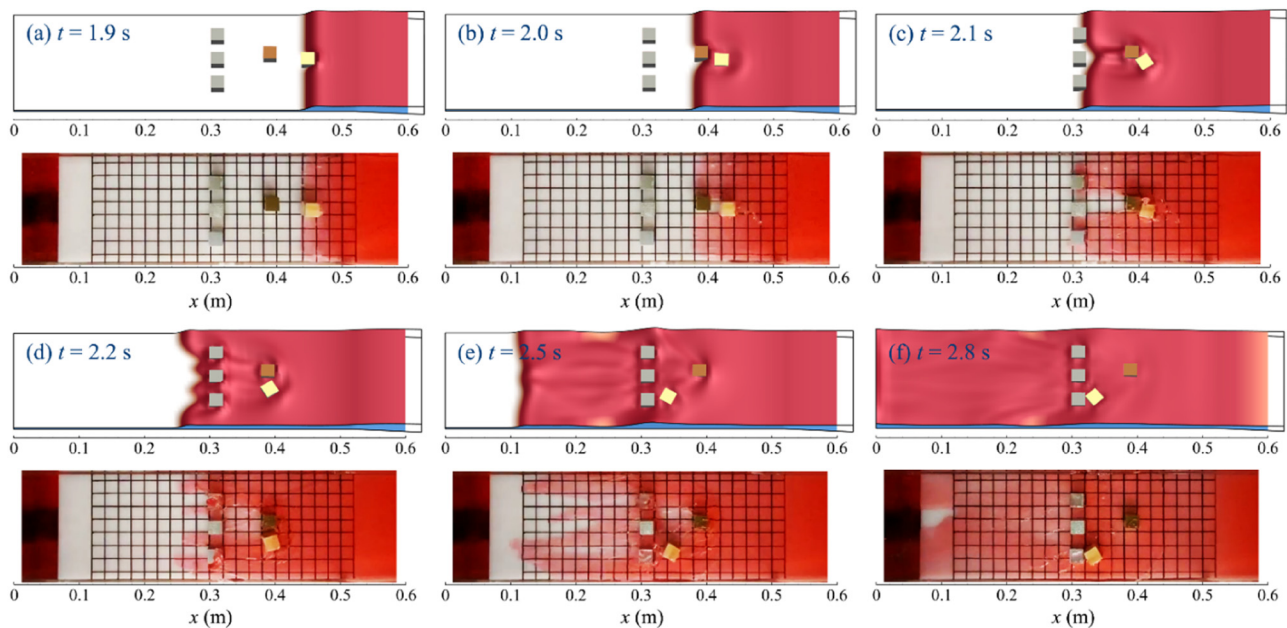


FIG. 19. Comparison of simulated moving trajectories of structures and wave–structure interaction flow field with experimental measurements.

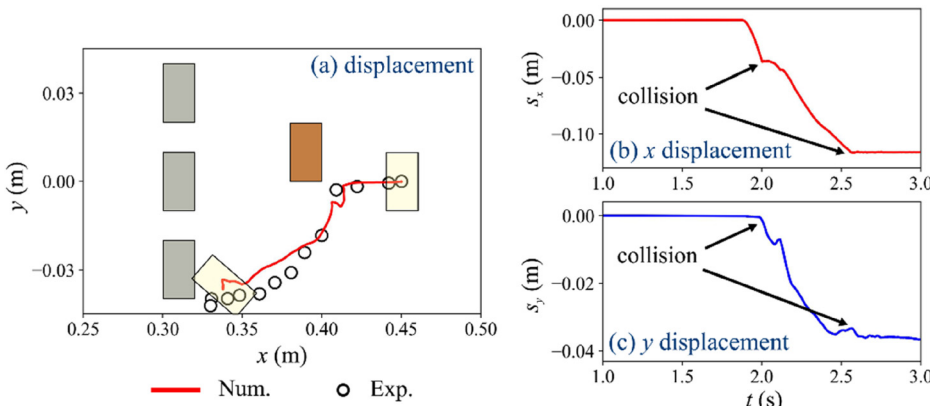


FIG. 20. Comparison of numerical and experimental time series of moving trajectory of the cubic centroid.

accurately captures the differences in dynamic response induced by two collision events. The initial collision (at $t = 2.0$ s) causes an abrupt change in direction of motion, while the secondary collision (at $t = 2.6$ s) results in a rapid dissipation of kinetic energy.

Overall, the numerical model effectively captures the macroscopic dynamic characteristics, despite its limitations in accurately modeling surface tension transitions and wet-dry friction changes as water flows over the plate surface. The model successfully simulates the collision process and dynamic responses under wave action, demonstrating its capability in predicting the kinetic behavior of structures in marine environments.

IV. CONCLUSION

In this paper, a numerical model coupled non-hydrostatic method with immersed boundary method is used to investigate the

issues of waves–structures interaction. The non-hydrostatic model employs a σ -coordinate transformation method to accurately simulate free surface dynamics, while the immersed boundary method effectively addresses structures within the flow field. To simulate the dynamic responses of rigid structures under wave loading, the numerical framework further incorporates rigid body dynamics and collision modeling, enhancing its capability in scenarios involving moving solid boundaries. Additionally, a novel water elevation correction method for virtual boundaries is proposed to address the mass conservation challenges of immersed boundary method during wave propagation over altering wet-dry structures.

The accuracy and stability of the numerical model are validated through a benchmark test case of linear waves propagating over a submerged bar. Comprehensive performance evaluations under complex wave–structure interaction scenarios have been conducted through

laboratory wave flume experiments. The capabilities of model in simulating wave generation, wave run-up, structural motion, and rigid body collision simulations have been evaluated systematically evaluated by a series of numerical cases. The numerical model successfully replicates mechanical wave generation process and accurately captures wave evolution processes. Motion trajectories of floating structures with varying densities under wave loading demonstrate good agreement with experimental measurements.

Through numerical simulations of wave run-up processes, this study comprehensively evaluates the performance of the numerical model in simulating wave interactions with stationary structures under complex free surface variations and topographical constraints. The numerical results demonstrate the sheltering patterns of structures and the attenuation effects of wave forces. Analysis based on the wave force attenuation coefficient reveals that structures in the front row can significantly reduce wave forces on downstream structures to 50% of the original values. As the number of structures increased, the attenuation effect stabilized, eventually maintaining a force reduction of approximately 15%. The numerical results show good agreement with theoretical predictions.

The model exhibits good competence in simulating free surface flow and wave–structure interactions. There are still some limitations in modeling wave breaking process and transient wet friction forces during water inundation over horizontal plates. Future improvements will focus on improved physical modeling of these processes. Overall, the numerical framework shows promising potential for extensive applications in coastal and ocean engineering, particularly in scenarios involving moving structures and their hydrodynamic interactions with waves.

ACKNOWLEDGMENTS

This work was sponsored by the National Natural Science Foundation of China (Grant No. U2441218). The authors would like to thank the editors and anonymous reviewers for their comments and suggestions to improve the manuscript.

AUTHOR DECLARATIONS

Conflict of Interest

The authors have no conflicts to disclose.

Author Contributions

Pengxuan Luo: Methodology (equal); Software (equal); Writing – original draft (equal). **Jingxin Zhang:** Funding acquisition (equal); Supervision (equal); Writing – review & editing (equal).

DATA AVAILABILITY

The data that support the findings of this study are available from the corresponding author upon reasonable request.

APPENDIX: WATER ELEVATION CORRECTION METHOD

In numerical modeling, the temporal variation of water elevation is governed by the mass conservation at each cell. However, the

virtual boundaries may induce discontinuities in vertical integration of governing equations under the σ coordinate, potentially compromising mass imbalance. Building on our previous methodology,⁴⁴ we implemented a water elevation correction method to address this problem.

This approach corrects the water elevation solution by constraining fluxes at virtual boundaries. Specifically, interfacial fluxes across IB cells are subject to physical constraints that prevent flow penetration through computational boundaries, thereby eliminating the issues of localized mass imbalance. Based on the discretized continuity governing equation for water elevation solving [Eq. (8) in Sec. II B] and the discretized momentum equation [Eq. (11) in Sec. II B], the water elevation correction method is implemented as follows:

$$\frac{\eta_{i,k}^* - \eta_{i,k}^n}{\Delta t} + \theta \sum_{k=1}^{NK} (\sigma_k \nabla \cdot \mathbf{q}_{i,k}^*) + (1 - \theta) \sum_{k=1}^{NK} (\sigma_k \nabla \cdot \mathbf{q}_{i,k}^n) = 0, \quad (A1)$$

$$\mathbf{q}_{i,k}^* = \mathbf{q}_{i,k}^{(1)} - \Delta t (\mathbf{D}_{i,k}^* + \theta g H \cdot \nabla \eta_{i,k}^*). \quad (A2)$$

First, the implicit diffusion term \mathbf{D} in Eq. (A2) is expanded and the implicit flux is shifted to the left side of the equation. Equations (A1) and (A2) can be summarized in the matrix notation for numerical solutions, which can be expressed as following forms:

$$\zeta_i^* + \mathbf{Z}_{1i} \left(\frac{\partial \mathbf{Q}_x}{\partial x} \right)_i^* + \mathbf{Z}_{1i} \left(\frac{\partial \mathbf{Q}_y}{\partial y} \right)_i^* = \zeta_i^n - \mathbf{Z}_{2i}^n \left(\frac{\partial \mathbf{Q}_x}{\partial x} \right)_i^n - \mathbf{Z}_{2i}^n \left(\frac{\partial \mathbf{Q}_y}{\partial y} \right)_i^n, \quad (A3)$$

$$\mathbf{A}_i^n \mathbf{Q}_x^* = \mathbf{Q}_x^{(1)} + \mathbf{B}_i^n \left(\frac{\partial \zeta}{\partial x} \right)_i^*, \quad (A4)$$

$$\mathbf{A}_i^n \mathbf{Q}_y^* = \mathbf{Q}_y^{(1)} + \mathbf{B}_i^n \left(\frac{\partial \zeta}{\partial y} \right)_i^*, \quad (A5)$$

where the coefficient matrix \mathbf{A} is a positive definite matrix, and the vector \mathbf{B} and \mathbf{Z} represent parameters have been calculated. The vector \mathbf{Q} contains the flux variables to be solved.

In order to solve the implicit terms of water elevation, Eqs. (A4) and (A5) are substituted into the continuity equation (A3) and it can be expressed by

$$\begin{aligned} \zeta_i^* + \mathbf{Z}_{1i} \left\{ \frac{\partial}{\partial x} \left[(\mathbf{A}^{-1})_i^n \mathbf{B}_i^n \left(\frac{\partial \zeta}{\partial x} \right)_i^* \right] + \frac{\partial}{\partial y} \left[(\mathbf{A}^{-1})_i^n \mathbf{B}_i^n \left(\frac{\partial \zeta}{\partial y} \right)_i^* \right] \right\} \\ = \zeta_i^n - \mathbf{Z}_{1i} \left\{ \frac{\partial}{\partial x} [(\mathbf{A}^{-1})_i^n \mathbf{Q}_x^{(1)}] + \frac{\partial}{\partial y} [(\mathbf{A}^{-1})_i^n \mathbf{Q}_y^{(1)}] \right\} \\ - \mathbf{Z}_{2i}^n \left[\left(\frac{\partial \mathbf{Q}_x}{\partial x} \right)_i^n + \left(\frac{\partial \mathbf{Q}_y}{\partial y} \right)_i^n \right]. \end{aligned} \quad (A6)$$

Based on the Gauss's divergence theorem, Eq. (A5) is integrated over the control volume of mesh cell i and all gradient terms derived in local coordinates. The implicit terms at left hand side (LHS) can be organized as

$$\begin{aligned} LHS_i^* &= \zeta_i^n A_i + Z_{1i} \sum_{j=1}^{NJ} \left\{ \frac{(\mathbf{A}^{-1} \mathbf{B}_1)_{ij}^n}{J_{ij}} \left[\frac{\zeta_{ij}^* - \zeta_i^*}{\Delta \xi_{ij}} y_{\eta ij} l_{ij} \cos \alpha_{ij} - \frac{\zeta_{ij}^* - \zeta_i^*}{\Delta \xi_{ij}} l_{ij} x_{\eta ij} \sin \alpha_{ij} \right] \right\} \\ &\quad + Z_{1i} \sum_{j=1}^{NJ} \left\{ \frac{(\mathbf{A}^{-1} \mathbf{B}_1)_{ij}^n}{J_{ij}} \left[\frac{\zeta_{ij}^* - \zeta_i^*}{\Delta \eta_{ij}} x_{\xi ij} l_{ij} \sin \alpha_{ij} - \frac{\zeta_{ij}^* - \zeta_i^*}{\Delta \eta_{ij}} y_{\xi ij} l_{ij} \cos \alpha_{ij} \right] \right\}, \end{aligned} \quad (\text{A7})$$

where j represents the surface index of cell, and the subscript ij represents the variables at the cell neighboring the surface j of cell i .

After integration, the explicit terms at right-hand side (RHS) actually represents the flux across the surface of cell i . Within the immersed boundary method implementation, flux constraints are applied at the interfaces of IB cells, which can be identified at each time step. The right-hand side of Eq. (A5) can be expressed as

$$\begin{aligned} RHS_i^* &= \zeta_i^n A_i - Z_{2i} \sum_{j=1}^{NJ} [\mathbf{Q}_{xij}^n l_{ij} (1 - \delta_{IB,j}) \cos \alpha_{ij} + \mathbf{Q}_{yij}^n l_{ij} (1 - \delta_{IB,j}) \sin \alpha_{ij}] \\ &\quad + Z_{1i} \sum_{j=1}^{NJ} \left[(\mathbf{A}^{-1} \mathbf{Q}_{xi})_{ij}^{(1)} l_{ij} (1 - \delta_{IB,j}) \cos \alpha_{ij} \right. \\ &\quad \left. + (\mathbf{A}^{-1} \mathbf{Q}_{yi})_{fij}^n l_{ij} (1 - \delta_{IB,j}) \sin \alpha_{ij} \right], \end{aligned} \quad (\text{A8})$$

where the subscript IB represents the index of IB cells. By incorporating Kronecker delta symbols with the term $(1 - \delta_{IB,j})$, which is vanished when the neighboring cell on surface j of cell i is a boundary cell, the flow flux through the interface can be

restricted to ensure that the flow cannot penetrate the virtual boundary.

Combining Eqs. (A7) and (A8), the water elevation can be obtained by solving a set of linear equations:

$$AP_i^n \zeta_i^* + \sum_{j=1}^{NJ} AP_{ij}^n \zeta_{ij}^* = AB_i^n, \quad (\text{A9})$$

where the coefficient in Eq. (A9) can be written as following forms:

$$\begin{aligned} AP_{ij}^n &= \frac{Z_{1i} (\mathbf{A}^{-1} \mathbf{B}_1)_{ij}^n}{J_{ij} \Delta \xi_{ij}} (y_{\eta ij} l_{ij} \cos \alpha_{ij} - x_{\eta ij} l_{ij} \sin \alpha_{ij}), \\ AP_i^n &= A_i - \sum_{j=1}^{NJ} AP_{ij}, \\ AB_i^n &= RHS_i^n - Z_{1i} \sum_{j=1}^{NJ} \left[\frac{(\mathbf{A}^{-1} \mathbf{B}_1)_{ij}^n}{J_{ij}} \cdot \frac{\zeta_{ij}^* - \zeta_i^*}{\Delta \eta_{ij}} \right. \\ &\quad \left. \times (x_{\xi ij} l_{ij} \sin \alpha_{ij} - y_{\xi ij} l_{ij} \cos \alpha_{ij}) \right]. \end{aligned} \quad (\text{A10})$$

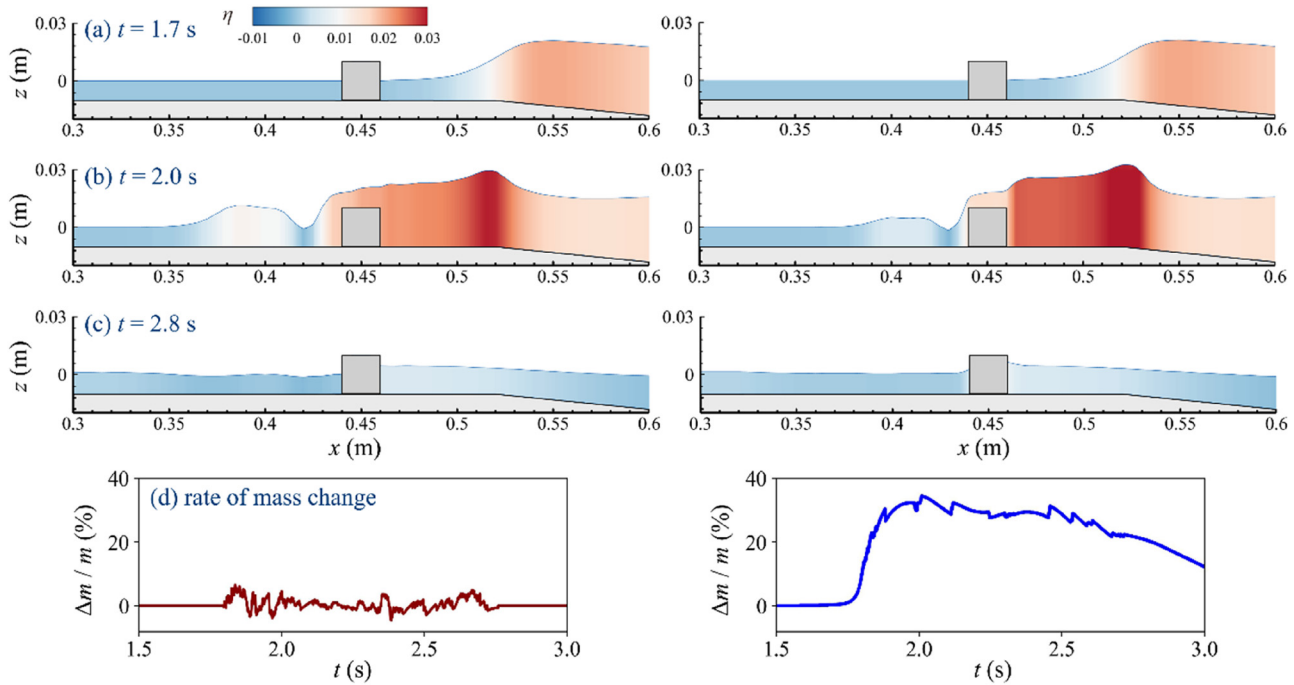


FIG. 21. Rate of mass change at the space occupied by structure during wave propagation. (Left: using water elevation correction method; right: without water elevation correction method).

By solving the Eq. (A9), the water elevation can be corrected and the hydrostatic boundary condition will be reconstructed.

A small-scale validation case is used to demonstrate the effectiveness of the water elevation correction method in improving mass conservation within the region occupied by a structure during wave propagating over the structure. Figure 21 presents a comparison of results obtained with and without the water elevation correction method under the wave conditions described in Sec. III C.

As shown in Fig. 21, the wave front has propagated to the leading edge of the structure at $t = 1.7$ s. At $t = 2.0$ s, as the wave propagate over the structure, the water elevation downstream obtained using the correction method is significantly higher than that without correction. A clear comparison in Fig. 21(d) reveals that without the water elevation correction, fluid penetrates the virtual boundary of the structure and preferentially fills the occupied space, causing an abnormal increase in fluid mass within this region. In contrast, applying the correction method effectively suppresses interface fluxes, maintaining relatively balanced fluid mass within the interior volume of structure.

REFERENCES

- ¹C. W. Hirt and B. D. Nichols, "Volume of fluid (VOF) method for the dynamics of free boundaries," *J. Comput. Phys.* **39**, 201–225 (1981).
- ²S. W. J. Welch and J. Wilson, "A volume of fluid based method for fluid flows with phase change," *J. Comput. Phys.* **160**(2), 662–682 (2000).
- ³S. Osher and R. P. Fedkiw, "Level set methods: An overview and some recent results," *J. Comput. Phys.* **169**(2), 463–502 (2001).
- ⁴F. Gibou, R. Fedkiw, and S. Osher, "A review of level-set methods and some recent applications," *J. Comput. Phys.* **353**, 82–109 (2018).
- ⁵J. Monaghan, "Smoothed particle hydrodynamics," *Annu. Rev. Astron. Astrophys.* **30**, 543–574 (1992).
- ⁶M. B. Liu and G. R. Liu, "Smoothed particle hydrodynamics (SPH): An overview and recent developments," *Arch. Comput. Methods Eng.* **17**(1), 25–76 (2010).
- ⁷P. Lin, "A multiple-layer σ -coordinate model for simulation of wave-structure interaction," *Comput. Fluids* **35**(2), 147–167 (2006).
- ⁸P. Lin and C. W. Li, "A σ -coordinate three-dimensional numerical model for surface wave propagation," *Int. J. Numer. Methods Fluids* **38**(11), 1045–1068 (2002).
- ⁹G. Ma, A. A. Farahani, J. T. Kirby, and F. Shi, "Modeling wave-structure interactions by an immersed boundary method in a σ -coordinate model," *Ocean Eng.* **125**, 238–247 (2016).
- ¹⁰G. Ma, F. Shi, and J. T. Kirby, "Shock-capturing non-hydrostatic model for fully dispersive surface wave processes," *Ocean Modell.* **43–44**, 22–35 (2012).
- ¹¹Z. Wei and Y. Jia, "Non-hydrostatic finite element model for coastal wave processes," *Coastal Eng.* **92**, 31–47 (2014).
- ¹²P. Smit, T. Janssen, L. Holthuijsen, and J. Smith, "Non-hydrostatic modeling of surf zone wave dynamics," *Coastal Eng.* **83**, 36–48 (2014).
- ¹³J. Zhang, A. N. Sukhodolov, and H. Liu, "Non-hydrostatic versus hydrostatic modelings of free surface flows," *J. Hydodyn.* **26**(4), 512–522 (2014).
- ¹⁴Y. Chen, Y. Chen, Z. Xu, P. Lin, and Z. Xie, "A double-layer non-hydrostatic model for simulating wave-structure and wave-jet interactions," *J. Comput. Phys.* **523**, 113634 (2025).
- ¹⁵C. Ai and S. Jin, "Non-hydrostatic finite volume model for non-linear waves interacting with structures," *Comput. Fluids* **39**(10), 2090–2100 (2010).
- ¹⁶D. Y. Choi, C. H. Wu, and C.-C. Young, "An efficient curvilinear non-hydrostatic model for simulating surface water waves," *Int. J. Numer. Methods Fluids* **66**(9), 1093–1115 (2011).
- ¹⁷E. Keilegavlen and J. Berntsen, "Non-hydrostatic pressure in σ -coordinate ocean models," *Ocean Modell.* **28**(4), 240–249 (2009).
- ¹⁸C. S. Peskin, "Flow patterns around heart valves: A numerical method," *J. Comput. Phys.* **10**, 252–271 (1972).
- ¹⁹D. Goldstein, R. Handler, and L. Sirovich, "Modeling a no-slip flow boundary with an external force field," *J. Comput. Phys.* **105**, 354–366 (1993).
- ²⁰E. A. Fadlun, R. Verzicco, P. Orlandi, and J. Mohd-Yusof, "Combined immersed-boundary finite-difference methods for three-dimensional complex flow simulations," *J. Comput. Phys.* **161**(1), 35–60 (2000).
- ²¹J. Mohd-Yusof, "Combined immersed-boundary/B-spline methods for simulations of flow in complex geometries," *Annual Research Briefs* (Center for Turbulence Research, NASA Ames and Stanford University, 1997), pp. 317–328.
- ²²Y. Tseng and J. H. Ferziger, "A ghost-cell immersed boundary method for flow in complex geometry," *J. Comput. Phys.* **192**(2), 593–623 (2003).
- ²³R. Mittal, H. Dong, M. Bozkurtas, F. M. Najjar, A. Vargas, and A. von Loebbecke, "A versatile sharp interface immersed boundary method for incompressible flows with complex boundaries," *J. Comput. Phys.* **227**(10), 4825–4852 (2008).
- ²⁴R. Mittal and G. Iaccarino, "Immersed boundary methods," *Annu. Rev. Fluid Mech.* **37**(1), 239–261 (2005).
- ²⁵C.-C. Liao and C.-A. Lin, "Simulations of natural and forced convection flows with moving embedded object using immersed boundary method," *Comput. Methods Appl. Mech. Eng.* **213–216**, 58–70 (2012).
- ²⁶M. Ehsan Khalili, M. Larsson, and B. Müller, "Immersed boundary method for viscous compressible flows around moving bodies," *Comput. Fluids* **170**, 77–92 (2018).
- ²⁷Z. Hao, B. Yin, M. Xu, and G. Yang, "A high-efficiency sharp-interface immersed boundary method based on multi-linear interpolation," *Phys. Fluids* **36**(9), 093617 (2024).
- ²⁸R. Verzicco, "Immersed boundary methods: Historical perspective and future outlook," *Annu. Rev. Fluid Mech.* **55**(1), 129–155 (2023).
- ²⁹L. Shen and E.-S. Chan, "Numerical simulation of nonlinear dispersive waves propagating over a submerged bar by IB-VOF model," *Ocean Eng.* **38**(2–3), 319–328 (2011).
- ³⁰L. Shen and E.-S. Chan, "Application of a combined IB-VOF model to wave-structure interactions," *Appl. Ocean Res.* **32**(1), 40–48 (2010).
- ³¹J. Yang and F. Stern, "Sharp interface immersed-boundary/level-set method for wave-body interactions," *J. Comput. Phys.* **228**(17), 6590–6616 (2009).
- ³²E. Zhao, J. Sun, Y. Tang, L. Mu, and H. Jiang, "Numerical investigation of tsunami wave impacts on different coastal bridge decks using immersed boundary method," *Ocean Eng.* **201**, 107132 (2020).
- ³³T. Ha, J. Shim, P. Lin, and Y.-S. Cho, "Three-dimensional numerical simulation of solitary wave run-up using the IB method," *Coastal Eng.* **84**, 38–55 (2014).
- ³⁴A. Kang, P. Lin, Y. J. Lee, and B. Zhu, "Numerical simulation of wave interaction with vertical circular cylinders of different submergences using immersed boundary method," *Comput. Fluids* **106**, 41–53 (2015).
- ³⁵C. Ai, Y. Ma, C. Yuan, and G. Dong, "A 3D non-hydrostatic model for wave interactions with structures using immersed boundary method," *Comput. Fluids* **186**, 24–37 (2019).
- ³⁶C. Ai, Y. Ma, C. Yuan, and G. Dong, "Non-hydrostatic model for internal wave generations and propagations using immersed boundary method," *Ocean Eng.* **225**, 108801 (2021).
- ³⁷X. Yu, Y. Shao, D. R. Fuhrman, and Y. Zhang, "A viscous numerical wave tank based on immersed-boundary generalized harmonic polynomial cell (IB-GHPC) method: Accuracy, validation and application," *Coastal Eng.* **180**, 104273 (2023).
- ³⁸F. R. Menter and Y. Egorov, "The scale-adaptive simulation method for unsteady turbulent flow predictions. Part 1: Theory and model description," *Flow, Turbul. Combust.* **85**(1), 113–138 (2010).
- ³⁹M. S. Darwish and F. Moukalled, "TVD schemes for unstructured grids," *Int. J. Heat Mass Transfer* **46**, 599–611 (2003).
- ⁴⁰S. Beiji and J. A. Battjes, "Experimental investigation of wave propagation over a bar," *Coastal Eng.* **19**, 151–162 (1993).
- ⁴¹J. P. Moris, A. B. Kennedy, and J. J. Westerink, "Tsunami wave run-up load reduction inside a building array," *Coastal Eng.* **169**, 103910 (2021).
- ⁴²T. Tomiczek, A. Prasetyo, N. Mori, T. Yasuda, and A. Kennedy, "Physical modelling of tsunami onshore propagation, peak pressures, and shielding effects in an urban building array," *Coastal Eng.* **117**, 97–112 (2016).
- ⁴³W. C. Moon, L. Q. Chiew, K. W. Cheong, Y. C. Tee, J. B. Chun, and T. L. Lau, "An experimental study for estimating tsunami wave forces acting on building with seaward and landward macroroughness," *Ocean Eng.* **186**, 106116 (2019).
- ⁴⁴P. Luo and J. Zhang, "An immersed boundary method coupled non-hydrostatic model for free surface flow," *Comput. Fluids* **275**, 106241 (2024).